
This is an electronic reprint of the original article.
This reprint may differ from the original in pagination and typographic detail.

Sun, D.-M.; Timmermans, M.Y.; Kaskela, A.; Nasibulin, A.G.; Kishimoto, Shigeru; Mizutani, Takashi; Kauppinen, E.I.; Ohno, Y.

Mouldable all-carbon integrated circuits

Published in:
Nature Communications

DOI:
[10.1038/ncomms3302](https://doi.org/10.1038/ncomms3302)

Published: 01/01/2013

Document Version
Publisher's PDF, also known as Version of record

Published under the following license:
CC BY

Please cite the original version:
Sun, D.-M., Timmermans, M. Y., Kaskela, A., Nasibulin, A. G., Kishimoto, S., Mizutani, T., Kauppinen, E. I., & Ohno, Y. (2013). Mouldable all-carbon integrated circuits. *Nature Communications*, 4, 1-8. Article 2302.
<https://doi.org/10.1038/ncomms3302>

ARTICLE

Received 18 Feb 2013 | Accepted 12 Jul 2013 | Published 6 Aug 2013

DOI: 10.1038/ncomms3302

OPEN

Mouldable all-carbon integrated circuits

Dong-Ming Sun^{1,†}, Marina Y. Timmermans², Antti Kaskela², Albert G. Nasibulin², Shigeru Kishimoto¹, Takashi Mizutani¹, Esko I. Kauppinen² & Yutaka Ohno^{1,3}

A variety of plastic products, ranging from those for daily necessities to electronics products and medical devices, are produced by moulding techniques. The incorporation of electronic circuits into various plastic products is limited by the brittle nature of silicon wafers. Here we report mouldable integrated circuits for the first time. The devices are composed entirely of carbon-based materials, that is, their active channels and passive elements are all fabricated from stretchable and thermostable assemblies of carbon nanotubes, with plastic polymer dielectric layers and substrates. The all-carbon thin-film transistors exhibit a mobility of $1,027 \text{ cm}^2 \text{ V}^{-1} \text{ s}^{-1}$ and an ON/OFF ratio of 10^5 . The devices also exhibit extreme biaxial stretchability of up to 18% when subjected to thermopressure forming. We demonstrate functional integrated circuits that can be moulded into a three-dimensional dome. Such mouldable electronics open new possibilities by allowing for the addition of electronic/plastic-like functionalities to plastic/electronic products, improving their designability.

¹Department of Quantum Engineering, Nagoya University, Furo-cho, Chikusa-ku, Nagoya, Aichi 464-8603, Japan. ²NanoMaterials Group, Department of Applied Physics and Center for New Materials, Aalto University, P.O. Box 15100, FI-00076 Aalto, Espoo, Finland. ³Multidisciplinary Institute of Digitalisation and Energy, Aalto University, P.O. Box 15100, FI-00076 Aalto, Espoo, Finland. † Present address: Advanced Carbon Division, Shenyang National Laboratory for Materials Science, Institute of Metal Research, Chinese Academy of Sciences, 72 Wenhua Road, Shenyang 110016, Liaoning, China. Correspondence and requests for materials should be addressed to Y.O. (email: yohno@nuee.nagoya-u.ac.jp).

Conventional integrated circuits (ICs) built on silicon wafers are rigid and fragile. However, recently, flexible devices have been fabricated on polymer films^{1,2}. In addition to flexibility, polymer materials exhibit plasticity or mouldability and can be permanently deformed into arbitrary shapes by applying mechanical force and heat. A variety of plastic products, ranging from those for daily necessities to electronics products and medical devices, are produced by such moulding techniques. However, neither the conventional semiconductor materials nor the electrodes/interconnections that comprise ICs can be moulded, owing to their poor stretchability and heat tolerance. Carbon nanotube (CNT) assemblies have excellent mechanical flexibility and stretchability as well as electric conductivity and heat tolerance. They have been used in various electronic and electromechanical devices, including flexible transparent conductive films^{3–5}, thin-film transistors (TFTs)^{6–10}, functional ICs^{8,9,11} and electromechanical sensors¹². Currently available carbon-based devices such as TFTs^{13–16} usually exhibit limited flexibility and stretchability owing to the use of rigid metal electrodes and oxide insulators (such as Al_2O_3 and SiO_2 , to name a few). Gate dielectrics made of polymers¹⁷ and ionic liquids¹⁸ have been introduced as alternatives; however, these usually result in high operating voltages and low operating speeds, respectively.

In this study, we demonstrate fully transparent and extremely stretchable TFTs and ICs that can operate at low voltages with a thick polymer gate insulator, utilizing the field focusing effect. We also show that these devices are mouldable via an air-assisted thermopressure-forming technique.

Results

All-carbon TFTs and ICs. We fabricated top-gate-type TFTs and ICs on a polyethylene naphthalate (PEN) substrate with a thickness of 125 μm . The active layer comprised a sparse network-like CNT thin film and the passive elements a dense 80-nm thick CNT thin film, with the dielectric and intermediate layers consisting of a 660-nm thick polymethyl methacrylate (PMMA) layer. We grew the CNTs using a floating-catalyst (aerosol) chemical vapour deposition technique¹⁹; collected them on a membrane filter, while controlling the CNT density to the appropriate level by adjusting the collection time; transferred the CNT film onto the substrate; and patterned it using standard photolithographic and oxygen plasma etching processes⁹. The average diameters of CNTs were evaluated from the optical absorption spectrum to be 1.1 nm for the channel⁹ and 1.4 nm for the electrodes and interconnections⁵. The CNT electrodes and interconnections exhibit a sheet resistance of $\sim 230 \Omega \text{sq}^{-1}$ and a transparency of 85% at a wavelength of 550 nm after being chemically doped with HNO_3 for 1 min.

As can be seen from Fig. 1a, the fabricated devices are fully transparent and flexible, with their transmittance being $\sim 10\%$ lower than that of the PEN substrate and reaching up to $\sim 80\%$ when 48% of the substrate is covered with the thick CNT film that forms the electrodes and the interconnections as shown in Fig. 1b. The colour map in the inset shows that the all-carbon ICs have less colour as compared with previously reported transparent devices based on oxides such as ZnO and indium tin oxide^{13,20}.

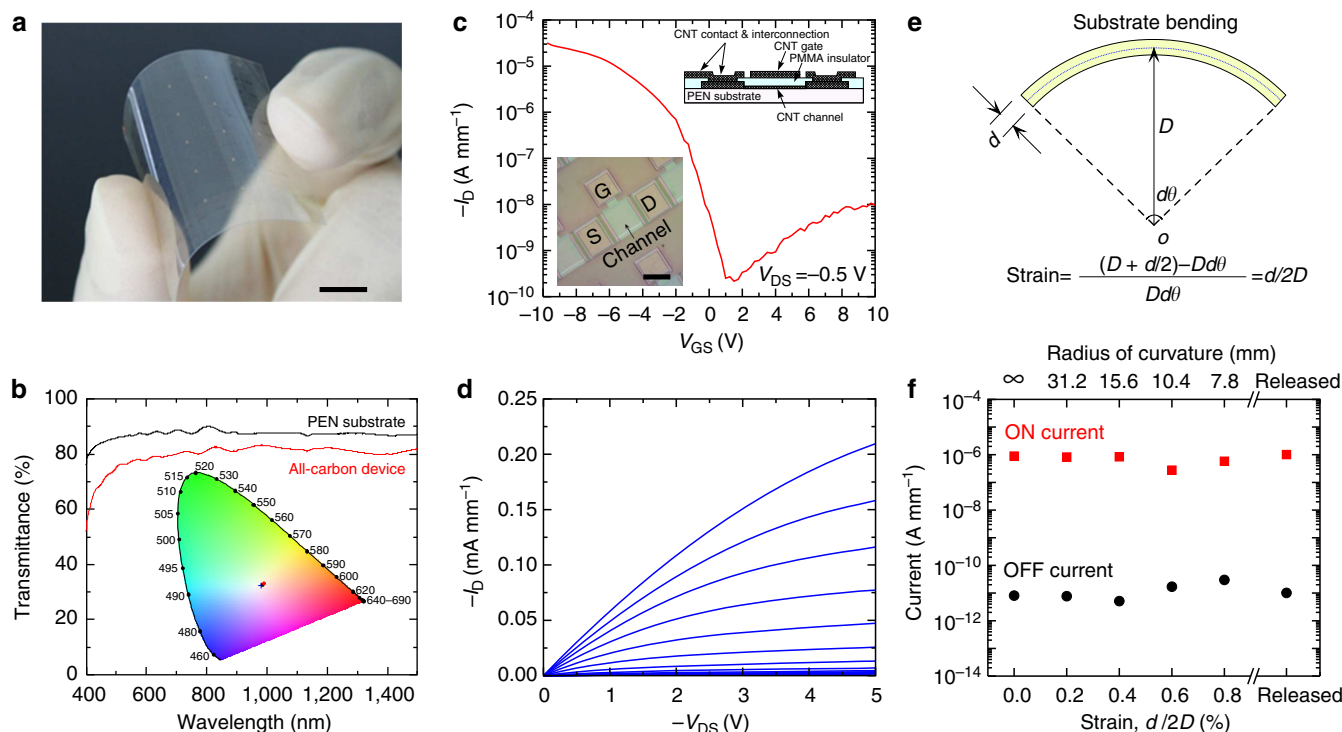


Figure 1 | Flexible and transparent all-carbon TFTs and ICs. (a) Photograph of an all-carbon device fabricated on a flexible PEN substrate (scale bar, 10 mm). (b) Optical transmittance of the PEN substrate (black line) and the device fabricated on the substrate (red line). Inset: plot showing the colour space (CIE 1931); the cross represents the colour white, and the black and red dots represent the colours of a bare PEN substrate and the all-carbon IC, respectively. (c) Transfer ($I_D - V_{GS}$) characteristics of an all-carbon top-gate TFT at $V_{DS} = -0.5$ V. $L_{ch} = W_{ch} = 100 \mu\text{m}$. Insets: optical micrograph of an all-carbon top-gate TFT array (bottom-left, scale bar, $100 \mu\text{m}$) and a schematic showing the cross-section of the all-carbon device (top-right). (d) Output ($I_D - V_{DS}$) characteristics of all-carbon TFT. V_{GS} was varied from -10 to 0 V in 1 -V steps. (e) Schematic showing a bent substrate. The radius of curvature, D , is measured from the point of origin, O , to the neutral axis of the substrate. The bending angle is $d\theta$. The linear strain is given by the equation. (f) The ON and OFF currents of the all-carbon TFT for the different bending levels.

Figure 1c shows the transfer characteristics of an all-carbon top-gate TFT. The channel length (L_{ch}) and channel width (W_{ch}) are both 100 μm . The device exhibits p-type characteristics with a high ON/OFF ratio of $>10^5$ and the subthreshold voltage of 0.73 V dec^{-1} . The effective device mobility was 1,027 $\text{cm}^2 \text{V}^{-1} \text{s}^{-1}$, which was evaluated in the linear region at $V_{\text{DS}} = -0.5 \text{ V}$ using the standard formula $\mu = (L_{\text{ch}}/W_{\text{ch}})(1/C)(1/V_{\text{DS}})(dI_{\text{D}}/dV_{\text{GS}})$. Here, C was estimated using a rigorous model that takes into account the realistic electrostatic coupling between the sparse CNTs and the gate electrode²¹. The mobility of the fabricated all-carbon TFTs exceeds not only those previously reported for CNT TFTs^{9,22} and low-temperature poly-Si TFTs^{23,24} but also that reported for single-crystal Si metal-oxide-semiconductor field-effect transistors²⁵. For C calculated using a parallel-plate model, that is, for $C = \epsilon/t_{\text{ox}}$, where ϵ is the dielectric constant of the gate insulator, the effective mobility is 321 $\text{cm}^2 \text{V}^{-1} \text{s}^{-1}$. Even for the high carrier mobility, the output saturation current density per unit device width (210 $\mu\text{A mm}^{-1}$ at $V_{\text{DS}} = -5 \text{ V}$, Fig. 1d) was still much smaller than conventional Si metal-oxide-semiconductor field-effect transistors. This is mainly due to the small gate capacitance composed by the thick PMMA gate insulator and low-density CNT channel. It is worth mentioning that the $I_{\text{D}} - V_{\text{DS}}$ characteristics exhibit ohmic behaviour in the linear region as shown in Fig. 1d, suggesting a formation of good ohmic contacts between the CNT channel and CNT electrodes.

As the all-carbon devices are made of CNTs and polymers, they exhibit better flexibility and stretchability compared with devices fabricated from rigid metals and oxide insulators. We performed the bending tests, in which the all-carbon devices were rolled, under various conditions, on cylinders having different diameters. When a substrate with a thickness (d) is bent with a radius of curvature (D) measured from the point of origin O to the natural axis of the substrate, the linear tensile strains of $d/2D$ is experienced by the outer surfaces of the devices as shown in Fig. 1e. The all-carbon TFTs exhibit only a small variation in the ON and OFF currents when subjected to bending strains of up to 0.8% as shown in Fig. 1f, thus demonstrating that the devices exhibited good flexibility.

We fabricated all-carbon ICs, including inverters; 11- and 21-stage ring oscillators; NOR, NAND and XOR gates; and static random access memory (SRAM) cells. The CNT electrodes and PMMA insulators were similar to those of the all-carbon TFTs. The load for the logic gates is a gate-source-shortened all-carbon

TFT. The channel width of the load TFTs is designed to be 50 μm , whereas that of the driver is 100 μm in order to adjust the thresholds of the logic gates. Figure 2a,b, respectively, show the photograph and circuit diagram and the oscillation waveform for a 21-stage all-carbon ring oscillator, in which 21 inverters are connected in series and with which an additional output buffer is integrated, resulting in the device having 44 TFTs in total. The output voltage begins oscillating spontaneously at a V_{DD} of -3 V . The oscillation frequency reaches a value of 3.0 kHz at a V_{DD} of -5 V , and the delay time for each inverter is 7.9 μs per gate, which is shorter than that for the ring oscillators with Au interconnections that we had reported previously⁹. Although the parasitic resistances of the CNT electrodes and interconnections are higher than those of metals, they do not significantly influence the delay times because the RC delay in switching is primarily caused by the ON resistance of the TFTs. The oscillation frequency of the ring oscillator is determined by the total gate delay of the inverters in the circuit chain. The delay time (τ) of each inverter can be approximated by the product of the total series resistance and the load capacitance (C_{load}) attributable to the gate of the inverter of the next stage. Thus, $\tau = \sum RC_{\text{load}}$ as shown in the simplified models in Fig. 2c. Here the resistance $\sum R$ includes the resistances of the CNTs and the interconnections (R_1 , R_2 , R_3 and R_4) and the ON resistances (R_{L} and R_{D}) of the TFTs. We estimated the resistances in the fabricated all-carbon devices to be $R_1 \sim 7 \text{ k}\Omega$, $R_2 \sim 1.5 \text{ k}\Omega$, $R_3 \sim R_4 \sim 15 \text{ k}\Omega$, $R_{\text{L}} \sim 2 \text{ M}\Omega$ and $R_{\text{D}} \sim 1 \text{ M}\Omega$, respectively, showing that the delay time is mostly determined by the channel resistance.

We also confirmed that the other functions of the ICs worked at V_{DD} of -5 V (Supplementary Fig. 1). It is worth mentioning that the various functions of the ICs could be tested at the fairly low voltage of -5 V even though a 660-nm thick polymer layer was used for the gate insulator in the TFTs. It is known that a thicker insulator usually leads to a higher operating voltage (tens of volts) in conventional Si-based TFTs and organic TFTs²⁶, because the gate-to-channel capacitance necessary for charging the carriers in the channel decreases in inverse proportion to the thickness of the gate insulator for a conventional two-dimensional (2D) channel. However, for a sparse network-like CNT thin film in which the spacings between the CNTs are large compared with the thickness of the gate insulator, the electrostatic coupling between the nanotubes and the gate electrode is enhanced because the electric force lines are focused on the

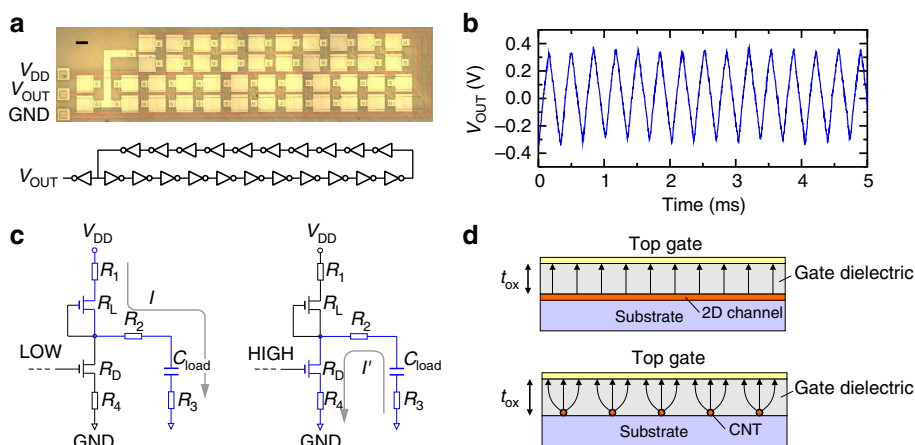


Figure 2 | 21-stage all-carbon ring oscillator. (a) Optical micrograph and circuit diagram (scale bar, 100 μm). (b) Oscillation waveform. (c) Schematic circuits showing charging (left) and discharging (right) processes in an inverter connected to the load capacitance. (d) Schematics showing the electric force lines in a 2D channel (top) and a sparse CNT channel (bottom). In the case of 2D channels found in conventional semiconductor TFTs, the electric force lines are uniformly distributed. On the other hand, in case of the sparse CNT thin film, in which the spacings between the CNTs are greater than the thickness of the gate insulator, the electric force lines are focused on the CNTs in the channel.

nanotubes, whose diameters are in the nanometre range, as shown in Fig. 2d. As a consequence, the gate-to-channel capacitance approximately becomes a function of $\log^{-1}(t)$, where t is the thickness of the gate insulator, leading to the gate-to-channel capacitance having a considerable value even for an increased gate insulator thickness, in contrast to what is noticed in 2D channels. On comparing the devices fabricated in this study with previously reported ones having inorganic gate insulators (Al_2O_3 ; t_{ox} : 40 nm; relative dielectric constant (ϵ_r): 10)⁹, the equivalent oxide layer thickness ($t_{\text{ox}}\epsilon_{\text{SiO}_2}/\epsilon_r$) for the present devices, which use PMMA as the gate insulator (t_{ox} : 660 nm; ϵ_r : 3.4), increases from 15.6 to 757 nm. Here, ϵ_{SiO_2} is relative dielectric constant of SiO_2 . For this case, the gate capacitance of the parallel-plate capacitor decreases to be 2%, whereas the capacitance of the sparse CNT channel is 41.5% of the initial value, resulting in an increase in the gate effect by a factor of 20.8. The low-voltage operation of the fabricated ICs is attributable to the sparse network-like CNT film.

The large gate-induced hysteresis typically observed in transfer characteristics of CNT transistors is one of the issues to be addressed. The present all-carbon TFTs exhibited relatively smaller hysteresis than previous CNT TFTs with a bottom gate structure⁹ (Supplementary Fig. S2). This is probably because the channel is covered with the PMMA gate insulator layer so as to decrease the amount of adsorbing ambient molecules such as water and oxygen causing hysteresis^{27–29}. Although the width of hysteresis increased with sweep amplitude of V_{GS} , in the range of

an operation voltage of present ICs ($V_{\text{DD}} = -5$ V), the hysteresis is still small enough to secure the noise margin for the logic operation as will be shown later.

Mouldability of all-carbon devices. The unique compositions of the devices allows them to be deformed in a three-dimensional (3D) manner using extremely high strains, which are induced via moulding using an air-assisted thermopressure-forming technique. This technique is shown schematically in Fig. 3a. The planar substrate is heated and blown to form a dome-shaped structure (Fig. 3b). The all-carbon device, as well as the PEN substrate, is then stretched biaxially during the forming process as shown in Fig. 3c. The process does not cause the CNT films to crack or peel, and the channel width and length both increase from 100 to 112 μm , corresponding to biaxial tensile strains of 12% (25% increase in area). This is in sharp contrast to rigid materials such as metals, which generally break down for strains greater than 1% (Supplementary Fig. S3). Moreover, the positions of upper layers such as the gate insulator and gate electrode did not shift relatively to the position of underlying drain/source and channel layers in the moulding process. The radii of curvature of the dome-shaped devices and the tensile strains induced in them can be controlled through the forming temperature as shown in Fig. 3d.

Figure 4a–f show the variations in the static characteristics of the all-carbon TFTs for a series of biaxial tensile strains with values up to 18.0%. The detail of the uniformity in the device

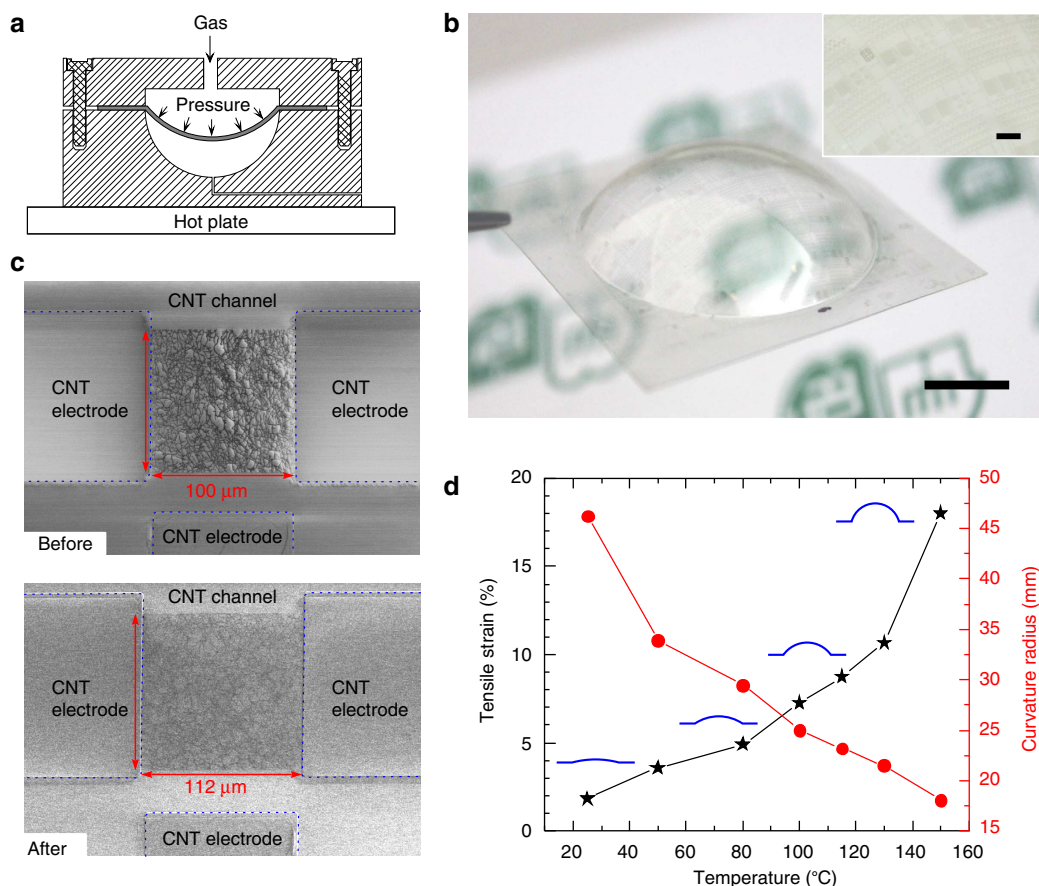


Figure 3 | Moulding of the all-carbon devices. (a) Schematic of the cross-section of the air-assisted thermopressure-forming apparatus. (b) Photograph of a dome-shaped all-carbon device (scale bar, 10 mm). Inset: magnified photograph (scale bar, 1 mm). (c) SEM images of the CNT channels and electrodes before and after the application of a biaxial tensile strain of 12% (scale bars, 100 μm). (d) Dependence on the forming temperature of the tensile strain and the corresponding radii of curvature.

property is shown in Supplementary Fig. S4. These TFTs were prepared using CNTs in two different densities; the lower density ($0.67 \text{ CNTs } \mu\text{m}^{-1}$) results in an initial ON/OFF ratio of $\sim 10^6$ (Fig. 4a), whereas the higher one ($1.34 \text{ CNTs } \mu\text{m}^{-1}$) leads to an initial ON/OFF ratio of $< 10^2$ (Fig. 4d). It is known that even if the metallic CNTs are incorporated in the channel in an amount of 30%, a high ON/OFF ratio can still be obtained by adjusting the density of the CNTs such that it is lower than the percolation threshold³⁰. On increasing the strain, the ON currents decrease slightly in both devices as shown in Fig. 4b,e. Consequently, the median mobility decreases from 675 to $311 \text{ cm}^2 \text{ V}^{-1} \text{ s}^{-1}$ for the lower CNT density (Fig. 4c) and from 1,168 to $935 \text{ cm}^2 \text{ V}^{-1} \text{ s}^{-1}$ for the higher one (Fig. 4f). We could notice two distinct trends in the OFF currents of the two devices. The ON/OFF ratio for the device with the lower CNT density remains constant at 10^6 , whereas it increases from 40 to 10^5 for the device with the higher CNT density.

These variations in the properties of the TFTs would be attributable to the decrease in the density of CNTs per unit area with the increase in the channel area. The increase in ON/OFF ratio of the higher-CNT-density device is caused by the density of metallic CNTs that become lower than the percolation threshold. We found no evidence to suggest that the channel CNTs are cut by the shearing force in effect at the interface between the CNTs and the surrounding polymer^{31,32} during the forming process. The noncovalent intermolecular interactions between the CNTs and the polymer are much weaker than covalent sp^2 carbon-carbon bonds^{33–35}. Furthermore, the shearing force decreases as the temperature increases. Because of the weak Van der Waals forces at the CNT/CNT junctions, the increase in the area of the CNT thin films is owing to the relative movements of the CNTs. In addition, the sheet resistance of CNT interconnections also increases by $\sim 60\%$ for a strain of 18%.

Demonstration of mouldable ICs. The all-carbon logic ICs also exhibit mouldability. We demonstrate this by using the CNT film with the higher density for the channel to ensure that the ICs function even after being moulded. Figure 5 shows the electrical performance of a moulded inverter with various biaxial tensile strain. The ON/OFF ratio of the driving TFT of the inverter increased from 30 to 2×10^4 (data not shown) at a strain of 7.2%.

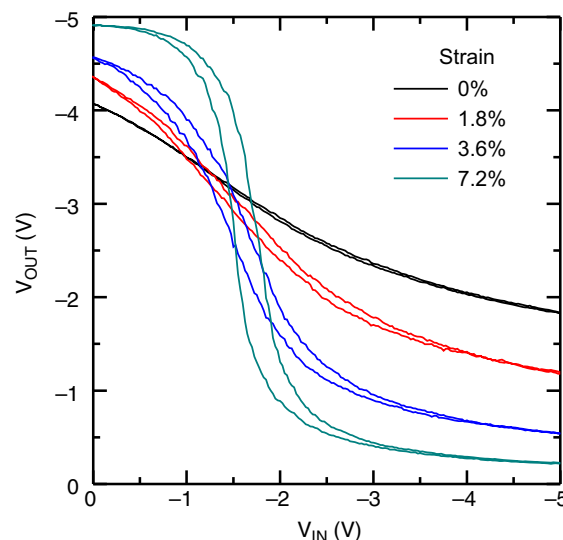


Figure 5 | Electrical performance of an inverter after it had been moulded. Transfer characteristics of an inverter moulded with biaxial tensile strains of 0, 1.8, 3.6 and 7.2%. $V_{DD} = -5 \text{ V}$.

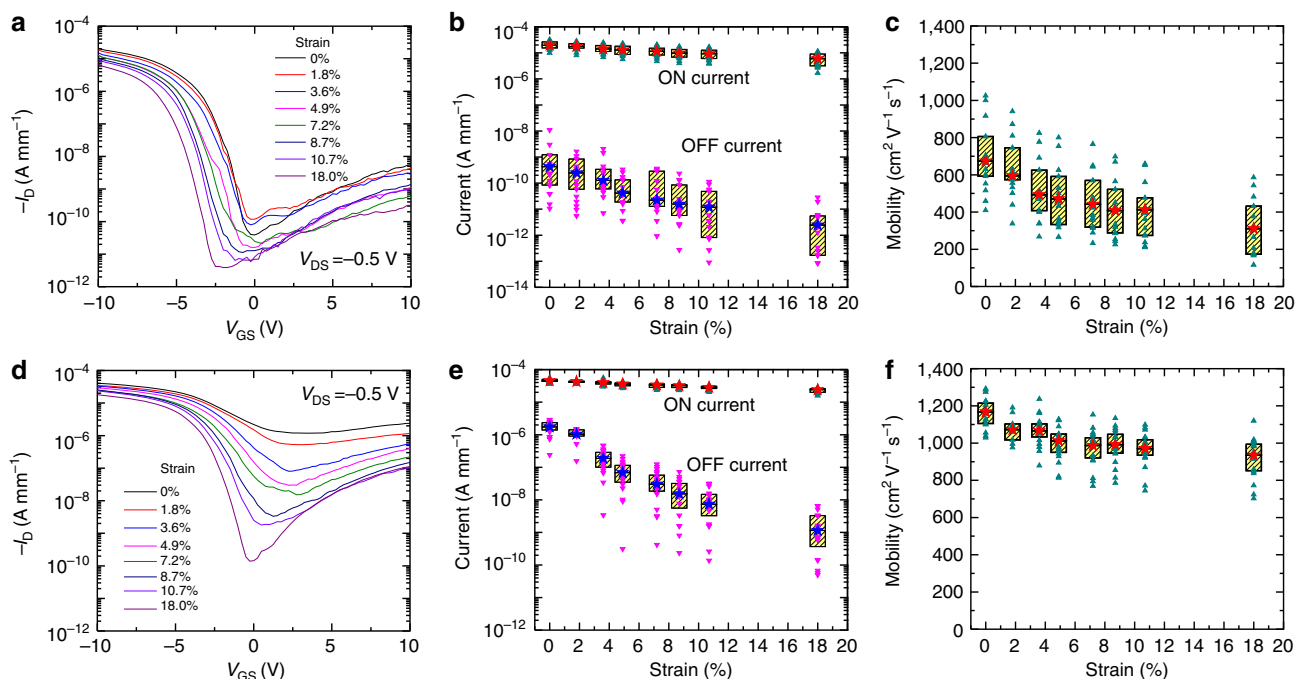


Figure 4 | Variation of property of all-carbon devices when subjected to moulding. (a–c) Transfer characteristics, ON and OFF currents, and mobilities of the all-carbon TFTs moulded under different conditions. The TFTs have a low-density channel, which leads to a high initial ON/OFF ratio. $V_{DS} = -0.5 \text{ V}$. $L_{ch} = W_{ch} = 100 \mu\text{m}$. The currents are normalized to the same unit (A mm^{-1}) because the channel dimensions increase after the moulding process. The ON and OFF currents and mobilities of 20 TFTs are plotted versus strain. The solid stars represent the median, and the upper and lower bands of the boxes correspond to the 75th and 25th percentiles, respectively, of the device population. (d–f) Transfer characteristics, currents and mobilities of the all-carbon TFTs moulded under different conditions. The TFTs have high-density channels, which lead to low initial ON/OFF ratios.

Accordingly, the output performance of the device shows a distinct improvement, with the output voltage swings increasing from -4.0 V and -1.8 V to -4.9 V and -0.2 V, respectively, and the voltage gain from 0.8 to 11, suggesting that such logic circuits can function even after being strained to this extent. Figure 6 shows the all-carbon ICs for an XOR gate (Fig. 6a–e) and an SRAM device (Fig. 6f–i), moulded such that they experience a 7.2% biaxial strain. The XOR gate, which represents the inequality function, consists of two inverters and three NAND gates, is operated by a clock (CLK) signal of 40 Hz and shows clear logic outputs with the large voltage swings.

SRAM is a type of memory that uses bistable latching circuitry to store each bit and is faster and more reliable than dynamic RAM. To our knowledge, the present device is the first SRAM fabricated using CNT-based transistors. The 1-bit all-carbon SRAM demonstrated consists of a pair of inverters and two access transistors. The folded transfer characteristics in Fig. 6h exhibit a large noise margin for the read and write operations of the SRAM, suggesting that the SRAM operates robustly during the write and read processes. This can also be seen from the time chart in Fig. 6i. When the word line (WL) is set to '1' to turn the

access transistors (T5 and T6) ON, the data D and \bar{D} are repeatedly written or read. Other logic gates that operate similarly under a biaxial strain of 7.2% are presented in Supplementary Fig. S5.

Discussion

Our demonstration of high-performance, low-voltage all-carbon TFTs and ICs opens new possibilities for transparent and flexible/stretchable electronics. Such low-voltage devices overcome the fundamental limits experienced by TFTs with 2D channels fabricated using thick polymers as insulators. This suggests that not only flexible/stretchable electronic devices but also printed ones, in which the printing of the gate insulator and low-voltage operations are usually difficult to achieve simultaneously, can be fabricated. More importantly, the mouldability of our all-carbon devices, owing to the extreme biaxial stretchability of both the passive and the active elements of the devices, could open the door for novel 3D electronic devices based on forming techniques that are used today to shape plastic products, and also allow electronic functionalities to be incorporated into plastic products at low cost.

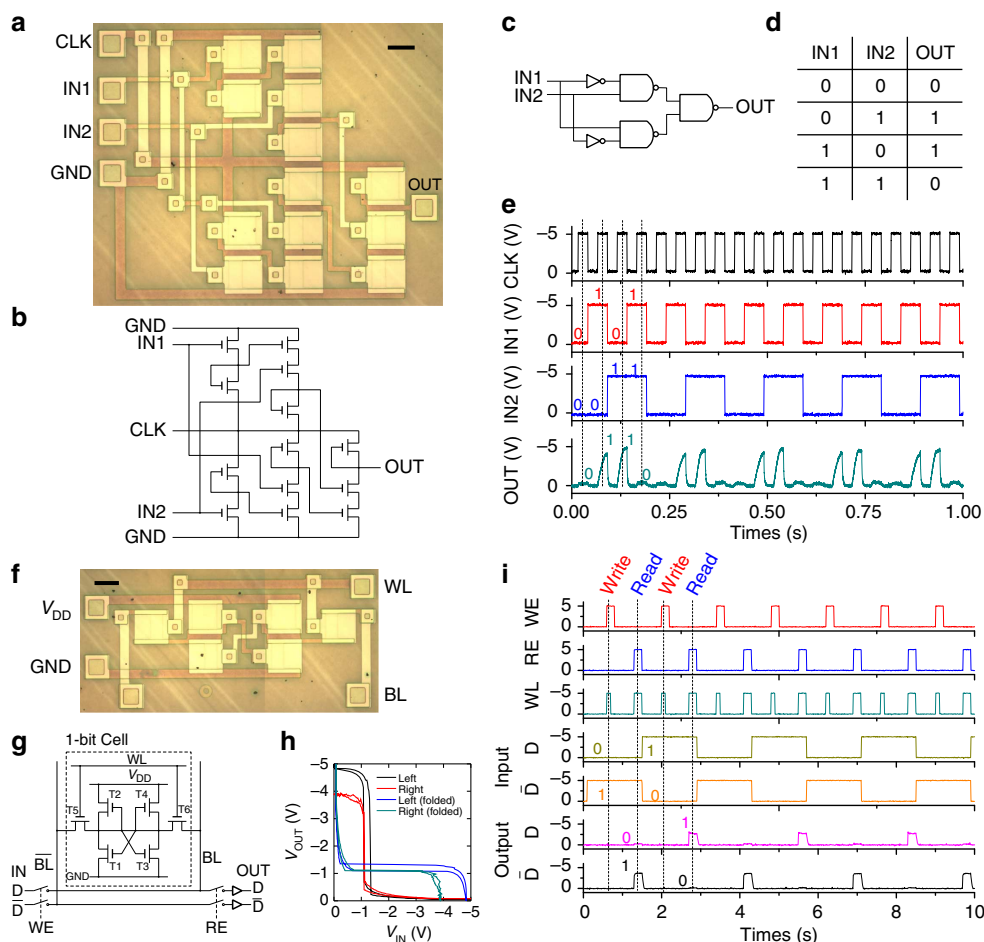


Figure 6 | Mouldable all-carbon ICs. (a–e) An XOR gate at a biaxial tensile strain of 7.2%. The panel includes an optical micrograph (scale bar, 100 μ m), circuit symbols (diagram), truth table and input-output characteristics in response to a clock (CLK) signal. **(f–i)** A 1-bit SRAM device at a biaxial strain of 7.2%. **(f,g)** Optical micrograph (scale bar, 100 μ m) and circuit diagram of the SRAM device. The two stable logic states of '0' and '1' are stored on four TFTs (T1, T2, T3 and T4), which form two cross-coupled inverters. Two additional access TFTs (T5 and T6) serve to control access to the storage cell during read and write operations. **(h)** Transfer characteristics of the two inverters measured at $V_{DD} = WL = -5$ V, which are folded to show a large noise margin. **(i)** Write and read operation of the 1-bit SRAM at $V_{DD} = WL = -5$ V. The data D and \bar{D} are written into the coupled inverters when 'Write enable' (WE) is set to '1' and are stored in the SRAM even if WE becomes '0'. The data D and \bar{D} can be read out (as shown in the bottom two panels) when 'Read enable' (RE) is set to '1'.

One of the major challenges that should be addressed for scaling up the CNT devices is the improvement of the performance variation of devices. The s.d. of ON current obtained in this work was $\sigma(I_{\text{ON}})/\langle I_{\text{ON}} \rangle = 0.32$ as shown in Supplementary Fig. S4a, which is about four time larger than that simulated for ideal random networks of CNTs with a constant length and conductivity. This suggests that the experimentally obtained variation is caused by the structural fluctuation of CNTs, and it is important to grow CNTs with a uniform length and diameter. For further improvement, metallic CNTs incorporated in the channel should be eliminated so that the density of CNTs is able to be increased without degrading ON/OFF ratio. Selective etching of metallic CNTs based on chemical³⁶, electrochemical³⁷, plasma³⁸ and light irradiation³⁹ methods would be applicable for present devices.

Methods

Device fabrication. First, metal marks (Ti/Au: 10/40 nm) were fabricated on a PEN (Teijin DuPont Films) substrate by standard photolithography, electron-beam evaporation and lift-off processes to aid in the alignment of the transparent CNT thin films. CNTs were grown using a floating-catalyst chemical vapour deposition technique and collected using a membrane filter. The dense CNT thin film for the source and drain electrodes and interconnections was transferred from the membrane filter to the substrate via a simple press transfer process⁵, and then patterned by photolithography and oxygen plasma etching processes. Next, a sparse CNT thin film to form the channels was transferred onto the substrate by dissolving the filter in acetone⁹. An insulator was formed on the substrate by spin coating a layer of PMMA (Microchem, 950 k MW) on it and baking the substrate on a hotplate at 170 °C for 1 h. The contact windows were formed by etching the PMMA insulator using acetone and a polydimethylglutarimide-based resist mask. Finally, another dense CNT film to form the gate electrodes was transferred onto the substrate and patterned using the same method as the one used to pattern the source and drain layer (See Supplementary Fig. S6 for the detail).

Moulding process. The fabricated all-carbon devices were fixed in the gas-moulding apparatus using screws. Compressed air at a pressure of 0.8 MPa was introduced into the moulding container, which was heated with a hotplate. After being heated for 5 min, the apparatus was allowed to cool to the room temperature, with the pressure of the compressed air being maintained.

Measurements. All electrical measurements were performed under ambient conditions. In order to test the logic ICs, function generators and oscilloscopes were used to generate the CLK and input signals and to observe the outputs, respectively. To prevent the input impedance of the oscilloscopes from interfering with the logic operations, high-impedance instrumental amplifiers were used as buffers. During the operation of the SRAM device, analogue switch ICs were also used to connect the bit lines to the input or output, depending 'Write enable' or 'Read enable' signals generated by a logic analyser.

References

- Kim, D. H. *et al.* Stretchable and foldable silicon integrated circuits. *Science* **320**, 507–511 (2008).
- Sekitani, T., Zschieschang, U., Klauk, H. & Someya, T. Flexible organic transistors and circuits with extreme bending stability. *Nature Mater.* **9**, 1015–1022 (2010).
- Wu, Z. C. *et al.* Transparent, conductive carbon nanotube films. *Science* **305**, 1273–1276 (2004).
- Hu, L., Hecht, D. S. & Gruner, G. Percolation in transparent and conducting carbon nanotube networks. *Nano Lett.* **4**, 2513–2517 (2004).
- Kaskela, A. *et al.* Aerosol-synthesized SWCNT networks with tunable conductivity and transparency by a dry transfer technique. *Nano Lett.* **10**, 4349–4355 (2010).
- Snow, E. S., Novak, J. P., Campbell, P. M. & Park, D. Random networks of carbon nanotubes as an electronic material. *Appl. Phys. Lett.* **82**, 2145–2147 (2003).
- Bradley, K., Gabriel, J. C. P. & Gruner, G. Flexible nanotube electronics. *Nano Lett.* **3**, 1353–1355 (2003).
- Cao, Q. *et al.* Medium-scale carbon nanotube thin-film integrated circuits on flexible plastic substrates. *Nature* **454**, 495–502 (2008).
- Sun, D. M. *et al.* Flexible high-performance carbon nanotube integrated circuits. *Nature Nanotech.* **6**, 156–161 (2011).
- Sangwan, V. K. *et al.* Fundamental performance limits of carbon nanotube thin-film transistors achieved using hybrid molecular dielectrics. *ACS Nano* **6**, 7480–7488 (2012).

- Wang, C. *et al.* Extremely bendable, high-performance integrated circuits using semiconducting carbon nanotube networks for digital, analog, and radio-frequency applications. *Nano Lett.* **12**, 1527–1533 (2012).
- Chaste, J. *et al.* A nanomechanical mass sensor with yoctogram resolution. *Nature Nanotech.* **7**, 300–303 (2012).
- Kim, S., Kim, S., Park, J., Ju, S. & Mohammadi, S. Fully transparent pixel circuits driven by random network carbon nanotube transistor circuitry. *ACS Nano* **4**, 2994–2998 (2010).
- Cao, Q. *et al.* Highly bendable, transparent thin-film transistors that use carbon-nanotube-based conductors and semiconductors with elastomeric dielectrics. *Adv. Mater.* **18**, 304–309 (2006).
- Jang, S. *et al.* Flexible, transparent single-walled carbon nanotube transistors with graphene electrodes. *Nanotechnol.* **21**, 425201 (2010).
- Yu, W. J. *et al.* Small hysteresis nanocarbon-based integrated circuits on flexible and transparent plastic substrate. *Nano Lett.* **11**, 1344–1350 (2011).
- Artukovic, E., Kaempgen, M., Hecht, D. S., Roth, S. & Gruner, G. Transparent and flexible carbon nanotube transistors. *Nano Lett.* **5**, 757–760 (2005).
- Ha, M. J. *et al.* Printed, sub-3V digital circuits on plastic from aqueous carbon nanotube inks. *ACS Nano* **4**, 4388–4395 (2010).
- Moisala, A. *et al.* Single-walled carbon nanotube synthesis using ferrocene and iron pentacarbonyl in a laminar flow reactor. *Chem. Eng. Sci.* **61**, 4393–4402 (2006).
- Fortunato, E., Barquinha, P. & Martins, R. Oxide semiconductor thin-film transistors: a review of recent advances. *Adv. Mater.* **24**, 2945–2986 (2012).
- Kang, S. J. *et al.* High-performance electronics using dense, perfectly aligned arrays of single-walled carbon nanotubes. *Nature Nanotech.* **2**, 230–236 (2007).
- Miyata, Y. *et al.* Length-sorted semiconducting carbon nanotubes for high-mobility thin film transistors. *Nano Res.* **4**, 963–970 (2011).
- Park, D. J., Kim, Y. H. & Park, B. O. High performance of ultralow temperature polycrystalline silicon thin film transistor on plastic substrate. *Solid State Electron.* **75**, 97–101 (2012).
- Jang, K., Lee, W., Choi, W. & Yi, J. High mobility P-channel thin-film transistors with ultralarge-grain polycrystalline silicon formed using nickel-induced crystallization. *Jpn J. Appl. Phys.* **51**, 09MF01 (2012).
- Sze, S. M. & Ng, K. K. *Physics of Semiconductor Devices* 3rd edn (John Wiley & Sons, Inc., 2007).
- Yan, H. *et al.* A high-mobility electron-transporting polymer for printed transistors. *Nature* **457**, 679–686 (2009).
- Kim, W. *et al.* Hysteresis caused by water molecules in carbon nanotube field-effect transistors. *Nano Lett.* **3**, 193–198 (2003).
- Shimauchi, H., Ohno, Y., Kishimoto, S. & Mizutani, T. Suppression of hysteresis in carbon nanotube field-effect transistors: Effect of contamination induced by device fabrication process. *Jpn J. Appl. Phys.* **45**, 5501–5503 (2006).
- Aguirre, C. M. *et al.* The role of the oxygen/water redox couple in suppressing electron conduction in field-effect transistors. *Adv. Mater.* **21**, 3087–3091 (2009).
- Kocabas, C. *et al.* Experimental and theoretical studies of transport through large scale, partially aligned arrays of single-walled carbon nanotubes in thin film type transistors. *Nano Lett.* **7**, 1195–1202 (2007).
- Sahoo, N. G., Rana, S., Cho, J. W., Li, L. & Chan, S. H. Polymer nanocomposites based on functionalized carbon nanotubes. *Prog. Polymer Sci.* **35**, 837–867 (2010).
- Frankland, S. J. V., Caglar, A., Brenner, D. W. & Griebel, M. Molecular simulation of the influence of chemical cross-links on the shear strength of carbon nanotube-polymer interfaces. *J. Phys. Chem. B* **106**, 3046–3048 (2002).
- Treacy, M. M. J., Ebbesen, T. W. & Gibson, J. M. Exceptionally high Young's modulus observed for individual carbon nanotubes. *Nature* **381**, 678–680 (1996).
- Salvetat, J. P. *et al.* Elastic and shear moduli of single-walled carbon nanotube ropes. *Phys. Rev. Lett.* **82**, 944–947 (1999).
- Bjork, J. *et al.* Adsorption of aromatic and anti-aromatic systems on graphene through pi-pi stacking. *J. Phys. Chem. Lett.* **1**, 3407–3412 (2010).
- Yang, C. M. *et al.* Selective removal of metallic single-walled carbon nanotubes with small diameters by using nitric and sulfuric acids. *J. Phys. Chem. B* **109**, 19242–19248 (2005).
- Wei, D. C. *et al.* Selective electrochemical etching of single-walled carbon nanotubes. *Adv. Funct. Mater.* **19**, 3618–3624 (2009).
- Zhang, G. Y. *et al.* Selective etching of metallic carbon nanotubes by gas-phase reaction. *Science* **314**, 974–977 (2006).
- Zhang, Y. Y., Zhang, Y., Xian, X. J., Zhang, J. & Liu, Z. F. Sorting out semiconducting single-walled carbon nanotube arrays by preferential destruction of metallic tubes using xenon-lamp irradiation. *J. Phys. Chem. C* **112**, 3849–3856 (2008).

Acknowledgements

This work was partially supported by Industrial Technology Research Grant Program in 2008 from New Energy and Industrial Technology Development Organization (NEDO)

of Japan; the R&D promotion scheme funding international joint research promoted by National Institute of Information and Communication Technology (NICT) of Japan; the Advanced Low Carbon Technology Research and Development Program of the Japan Science and Technology Agency; a Grant-in-Aid for Scientific Research from the Japan Society for the Promotion of Science; the Aalto University MIDE program via the CNB-E project; the Aalto University AEF program via the MOPPI project; and by the Academy of Finland (Pr. No. 128445).

Author contributions

Y.O. and E.I.K. conceived and designed the experiments. D.-M.S. and Y.O. designed, fabricated and characterized the TFTs and ICs. M.Y.T. and A.K. grew the carbon nanotubes. A.G.N. and E.I.K. developed the floating-catalyst growth technique. D.-M.S. and Y.O. co-wrote the paper. All the authors discussed the results and commented on the manuscript.

Additional information

Supplementary Information accompanies this paper at <http://www.nature.com/naturecommunications>

Competing financial interests: The authors declare no competing financial interests.

Reprints and permission information is available online at <http://npg.nature.com/reprintsandpermissions/>

How to cite this article: Sun, D.-M. *et al.* Mouldable all-carbon integrated circuits. *Nat. Commun.* 4:2302 doi: 10.1038/ncomms3302 (2013).



This work is licensed under a Creative Commons Attribution-NonCommercial-ShareAlike 3.0 Unported License. To view a copy of this license, visit <http://creativecommons.org/licenses/by-nc-sa/3.0/>